AD-A149 406 GAALASSB APD OPTIMIZATION(U) ROCKWELL INTERNATIONAL 1/1
THOUSAND OAKS CA MICROELECTRONICS RESEARCH AND
DEVELOPMENT CENTER R CHIN OCT 84 MRD41113.4FR
UNCLASSIFIED RADC-TR-84-191 F19628-82-C-0005 F/G 19/1 NL

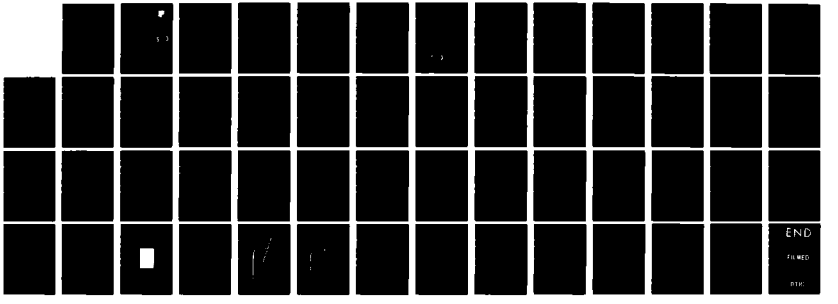

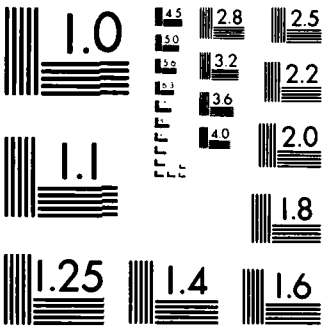

12

RADC-TR-84-191
Final Technical Report
October 1984

GaA1AsSb APD OPTIMIZATION

Rockwell International

R. Chin

APPROVED FOR PUBLIC RELEASE; DISTRIBUTION UNLIMITED

ROME AIR DEVELOPMENT CENTER
Air Force Systems Command
Griffiss Air Force Base, NY 13441

This report has been reviewed by the RADC Public Affairs Office (PA) and is releasable to the National Technical Information Service (NTIS). At NTIS it will be releasable to the general public, including foreign nations.

RADC-TR-84-191 has been reviewed and is approved for publication.

APPROVED: Thomas G. Ryan

THOMAS G. RYAN
Project Engineer

APPROVED: Harold Roth

HAROLD ROTH, Director
Solid State Sciences Division

FOR THE COMMANDER: John A. Ritz

JOHN A. RTIZ
Acting Chief, Plans Office

If your address has changed or if you wish to be removed from the RADC mailing list, or if the addressee is no longer employed by your organization, please notify RADC (ESO) Hanscom AFB MA 01731. This will assist us in maintaining a current mailing list.

Do not return copies of this report unless contractual obligations or notices on a specific document requires that it be returned.

REPORT DOCUMENTATION PAGE

1a. REPORT SECURITY CLASSIFICATION: UNCLASSIFIED	1b. RESTRICTIVE MARKINGS: N/A
2a. SECURITY CLASSIFICATION AUTHORITY: N/A	3. DISTRIBUTION/AVAILABILITY OF REPORT: Approved for public release; distribution unlimited.
2b. DECLASSIFICATION/DOWNGRADING SCHEDULE: N/A	
4. PERFORMING ORGANIZATION REPORT NUMBER(S): MRD41113.4FR	5. MONITORING ORGANIZATION REPORT NUMBER(S): RADC-TR-84-191
6a. NAME OF PERFORMING ORGANIZATION: Rockwell International; 6b. OFFICE SYMBOL (If applicable):	7a. NAME OF MONITORING ORGANIZATION: Rome Air Development Center (ESO)
6c. ADDRESS (City, State and ZIP Code): Microelectronics Research & Development Cntr, Thousand Oaks CA 91360	7b. ADDRESS (City, State and ZIP Code): Hanscom AFB MA 01731
8a. NAME OF FUNDING/SPONSORING ORGANIZATION: Rome Air Development Center; 8b. OFFICE SYMBOL (If applicable): ESO	9. PROCUREMENT INSTRUMENT IDENTIFICATION NUMBER: F19628-82-C-0005
8c. ADDRESS (City, State and ZIP Code): Hanscom AFB MA 01731	10. SOURCE OF FUNDING NOS.

PROGRAM ELEMENT NO.	PROJECT NO.	TASK NO.	WORK UNIT NO.
62702F	4600	19	33

11. TITLE (Include Security Classification): GaAlAsSb APD Optimization

12. PERSONAL AUTHOR(S): K. Chin

13a. TYPE OF REPORT	13b. TIME COVERED	14. DATE OF REPORT (Yr., Mo., Day)	15. PAGE COUNT
Final	FROM May82 TO Aug83	October 1984	56

16. SUPPLEMENTARY NOTATION: N/A

Io to the 1.5 power curve

17. COSATI CODES		
FIELD	GROUP	SUB GR
17	02	
09	01	

18. SUBJECT TERMS (Continue on reverse if necessary and identify by block number): Avalanche Photodiodes; Ionization Coefficient Enhancement

19. ABSTRACT (Continue on reverse if necessary and identify by block number)

It has been demonstrated that avalanche gain can be obtained in GaAlSb avalanche photodiodes which exhibit ionization coefficient enhancement. These devices exhibit gain at relatively high impurity background density of 8-9 x ~~10^{15}~~ cm^{-3}. This indicates that a tunneling process which occurs in these devices is associated with a deep level rather than a band-to-band process. Surface leakage current, which dominates the total dark current of these avalanche photodiodes at room temperature, can be reduced with the use of special structures. However, as shown in this work through both modeling and experiment, defect assisted tunneling may be a fundamental limitation to obtaining high sensitivity devices. Finally, a serious problem from the manufacturing standpoint is the necessity to compensate the native defect that results in a high concentration of intrinsic p-type acceptor levels. Precise control of dopant incorporation is required to reproducibly obtain the required net impurity levels. This is an extremely difficult process with the available LPE GaAlSb materials technology.

20. DISTRIBUTION/AVAILABILITY OF ABSTRACT	21. ABSTRACT SECURITY CLASSIFICATION
UNCLASSIFIED UNLIMITED ☒ SAME AS RPT. ☐ DTIC USERS ☐	UNCLASSIFIED

22a. NAME OF RESPONSIBLE INDIVIDUAL	22b. TELEPHONE NUMBER (Include Area Code)	22c. OFFICE SYMBOL
Thomas G. Ryan	(617)861-5590	RADC (ESO)

DD FORM 1473, 83 APR — EDITION OF 1 JAN 73 IS OBSOLETE.

1.0 Introduction and Summary 4

2.0 Technical Issues 6

2.1 Problem Statement 6

2.2 GaAlSb/GaSb Materials Systems 7

2.3 Materials Technologies 9

2.3.1 Liquid Phase Epitaxy 9

2.3.2 Metalorganic Chemical Vapor Deposition 11

2.4 APD Design and Performance 15

2.4.1 Basic Design Consideration of an Avalanche Photodiode 15

3.0 Experimental Data and Results 20

3.1 MOCVD GaAlSb Detector Data 20

3.2 Tunneling Data 25

3.3 1.55 Micron GaAlSb Avalanche Photodetectors 35

4.0 Summary 49

Fig. 2.2.1 Energy bandgap lattice constant diagrams of lattice matched III-V alloys near 1.3 micron 8

Fig. 2.3.1 Schematic diagram of a MOCVD system 14

Fig. 3.2.1 Temperature dependent I-V characteristic of Be-implanted GaAlSb photodiode 28

Fig. 3.2.2 The variation of $(C_2)^{2/3}$ with temperature 32

Fig. 3.2.3 Dark I-V showing I_{g-r} and I_{tun} 34

Fig. 3.3.1 Rocking curve of a GaAlSb epilayer grown upon GaSb 36

Fig. 3.3.2 Photoresponse vs. wavelength of a Schottky barrier GaAlSb avalanche photodetector 37

Fig. 3.3.3 Dark and illuminated I-V characteristic of a Schottky barrier avalanche photodiode showing gains in excess of thirty 39

Fig. 3.3.4 Photoresponse of the device of Fig. 3.3.3 to a linear light scan 40

Fig. 3.3.5 Temperature dependent I-V characteristics of a GaAlSb ($E_g \cong 0.80$ eV) avalanche photodiode 42

Fig. 3.3.6 Temperature dependent I-V characteristic of a second GaAlSb ($E_g \cong 0.80$ eV) avalanche photodiode 43

Fig. 3.3.7 GaAlSb Schottky avalanche breakdown voltage as a function of temperature 44

Fig. 3.3.8 110°K reverse I-V characteristic of a GaAlSb ($E_g \cong 0.80$ eV) avalanche photodiode 47

PREFACE

This report was prepared by Rockwell International/Microelectronics Research and Development Center under Contract No. F19628-82-C-0005.

The principal investigator and program manager for this project was Dr. Raymond Chin. The program manager for this project from RADC-Hanscom Field was Dr. Kenneth Soda. We wish to thank Professor G. E. Stillman of the University of Illinois and his students for their contributions to this program.

1.0 Introduction and Summary

The development of optical fibers with low loss and near zero wavelength dispersion in the wavelength region from 1.2 to 1.7 microns has served as the driving force for the development of low-noise, high-speed photodetectors in this region. To achieve the full potential of optical fiber systems, optical detectors must exhibit high quantum efficiency, low capacitance, low noise, high speed, and be readily manufacturable. For various military applications, radiation hardness is also a required characteristic.

One of the promising detectors which may meet all of these requirements is the GaAlSb avalanche photodiode. In this program, we have addressed the major issues which effect the performance of this device. Issues such as capacitance, sources of leakage current, and impurity density were addressed, to determine whether performance enhancement could be effected through device design or whether fundamental limitations, such as tunneling-dominated leakage current, existed. In addition, devices fabricated from material with the composition adjusted for ionization coefficient enhancement were fabricated and characterized to address these issues.

It has been demonstrated that avalanche gain can be obtained in 1.55 micron GaAlSb avalanche photodiodes. For this particular composition, the ionization coefficient ratio α/β is decreased resulting in lower excess noise. These devices also exhibit gain at a relatively high impurity background density of 8-9 x 10^{15} cm^{-3}. This indicates that tunneling, which also occurs in

InGaAsP photodiodes, as a band-to-band process, occurs through a deep level in this material. Surface leakage current dominates the total dark current, of these devices, at room temperature. This can be reduced with the use of special device structures. However, as shown in this work through modeling and experiment, the defect assisted tunneling may be a fundamental limitation to obtaining high sensitivity devices. Finally, one other serious problem from the manufacturing standpoint is the necessity to compensate the native defect that results in a high concentration of intrinsic p-type acceptor levels. Precise control of dopant incorporation is required to reproducibly obtain the required impurity levels. This is difficult to achieve using the presently available GaSb materials growth technology.

2.0 Technical Issues

2.1 Problem Statement

The development of optical fibers with low loss and near zero wavelength dispersion in the wavelength region from 1.2 to 1.7 microns has served as the driving force for the development of low-noise, high speed photodetectors in this region. To utilize the full potential of optical fiber systems, the optical detectors must have high quantum efficiency, low capacitance, low noise, wide bandwidth, and be readily manufacturable. For various military applications, radiation hardness is also a required characteristic. In the wavelength region of interest, three different semiconductor materials can be used. They are the elemental semiconductor Ge and the compounds GaInAsP and GaAlAsSb. Of these, both the GaInAsP and GaAlAsSb systems produce detectors which will operate at data rates greater than one gigabit per second. Only GaAlAsSb, however, is radiation hard. In addition, it has been demonstrated that the solid solution $Ga_{0.94}Al_{0.06}Sb$ has low excess noise associated with the carrier avalanche process. Therefore, the GaAlSb detector satisfies most requirements as a detector for use in military fiber optic systems.

In addition to the advantageous materials properties of GaAlSb, the performance characteristics of the devices fabricated from this semiconductor must satisfy given specifications. Detectors for optical fiber systems, exclusive of the base material, must exhibit low capacitance, low excess noise, small dark current, high speed, and reasonable gain.

High speed operation, in excess of 1 Gbit/sec, and low excess noise have been demonstrated for avalanche photodiodes fabricated from GaAlSb. To date, however, the leakage current and capacitance of GaAlSb devices have not been sufficiently low to offer an overall device performance advantage as compared to detectors fabricated in other material systems. In this study, we address the issues of GaAlSb avalanche photodiode leakage current, capacitance, surface passivation, device design, and design optimization to determine whether a "properly" fabricated GaAlSb photodiode will offer performance advantages as compared to other detectors.

2.2 GaAlSb/GaSb Materials Systems

The GaAlSb/GaSb materials system is qualitatively very similar to the well developed GaAlAs/GaAs materials systems. For small AlSb mode fractions, GaAlSb has a fairly good lattice match to GaSb. The addition of As to GaAlSb allows the resultant GaAlAsSb alloy to be exactly lattice-matched to GaSb over a wide range of compositions. The diagram of Fig. 2.2.1 shows that energy gap GaAlAsSb can cover a wide range when lattice matched to GaSb. The system is similar to the GaAlAs ternary system in that the energy gap can be altered by the addition of Al with little change in the lattice constant.

To date, both LPE and MOCVD have been used to grow GaAlSb and GaAlAsSb. Unintentionally doped GaAlSb or GaAlAsSb grown by either method is typically p-type except for LPE growth at very low growth temperature (< 400°C). The

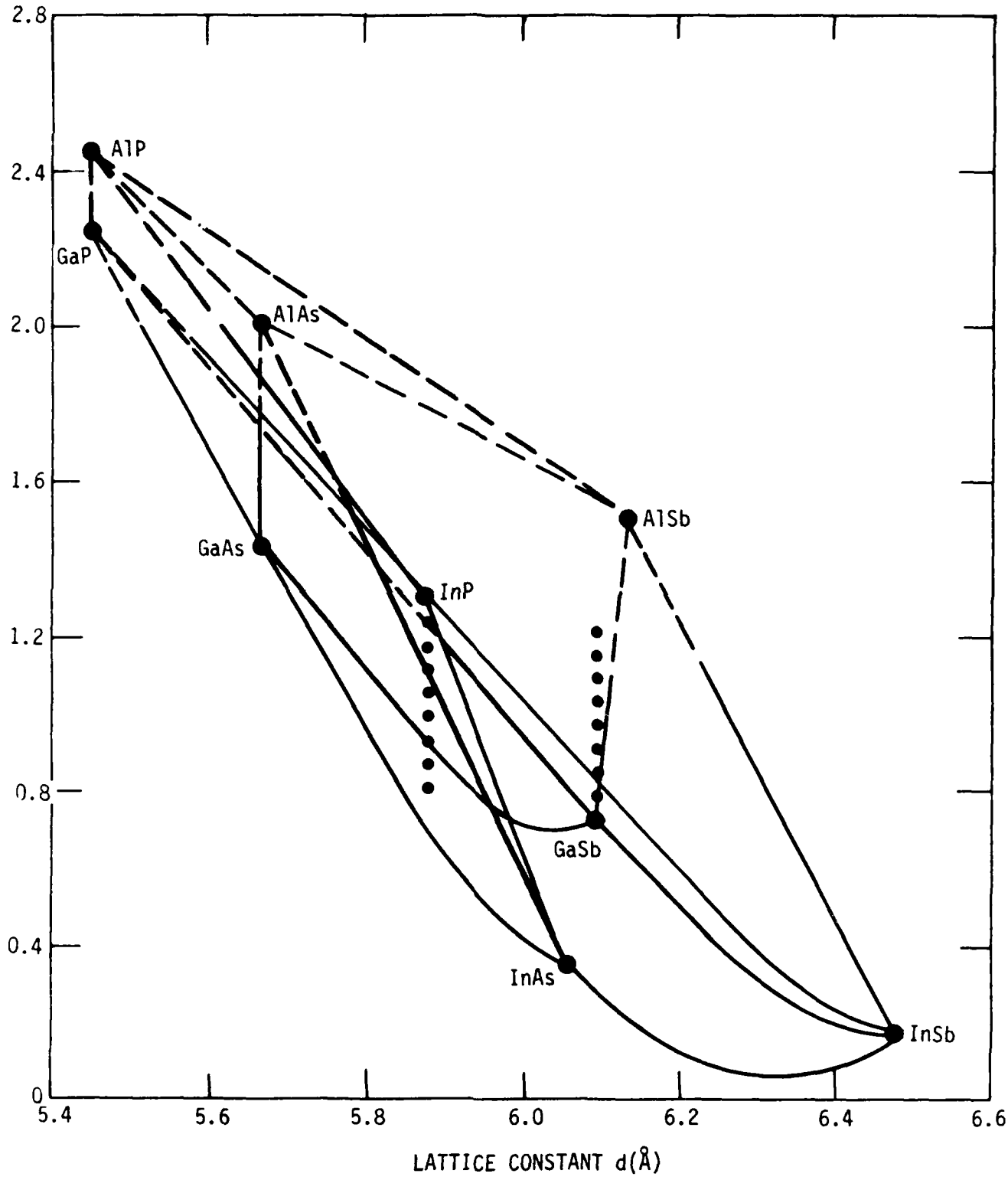

Fig. 2.2.1 Energy bandgap lattice constant diagrams of lattice matched III-V alloys near 1.3 micron.

p-type character has been attributed to Sb vacancies. Depending on the growth temperature, aluminum composition, and the growth rate, the net acceptor concentration ranges from 1×10^{16} to 2×10^{17} cm^{-3}. Tellurium can be used to dope the layers n-type; however, both carrier concentration and conductivity type will vary based on the Te concentration. The large number of factors which control the electrical properties of the GaAlSb solid solutions require extensive doping calibration for each alloy composition and growth temperature.

2.3 Materials Technologies

In recent years, the crystal growth art of III-V semiconductors has progressed to a well-developed technology. Various epitaxial growth methods such as liquid phase epitaxy, metalorganic chemical vapor deposition, trichloride transport vapor phase epitaxy, solution growth LPE, and molecular beam epitaxy have been investigated. In this section, we discuss the methods of liquid phase epitaxy and metalorganic chemical vapor deposition used in this program.

2.3.1 Liquid Phase Epitaxy

The growth of III-V alloys by liquid phase epitaxy is probably the most widely used method. Basically, the growth solution is prepared by saturating a melt with constituents, including the dopant at a suitable growth temperature. The melt is then brought in contact with the substrate either at the saturation temperature or at some lower temperature corresponding to supersaturation of

the melt. The furnace temperature is either ramped down or kept constant to provide a driving force so that the elements in the melt will precipitate on the substrate in single crystal form.

The most outstanding advantages of the liquid phase epitaxy method is the purity of the grown material and the high quality of the layers. The impurities incorporated in the growth are "filtered" out by several factors. First, the impurities that exist in the whole growth system including the impurities in the melt can be baked out (volatilized) in a purified H_2 atmosphere. Then, the residual impurities of the environment are limited by their solubility in the melt. Furthermore, the crystal impurities from the growth are further filtered by their distribution coefficients which are usually less than unity. Consequently, the total residual impurity concentration in the solid, $N_D + N_A$, is usually the lowest among all the epitaxial growth methods. Correspondingly, the mobility of electrons in these crystals is usually the highest.

Another advantage of the LPE method is that the substrate can be etched in-situ prior to epitaxial deposition. For example, InP substrates are usually etched in-situ and regrown. This provides an extremely clean crystalline surface free of contaminants and thermal erosion. Uniform nucleation of the epitaxial material is obtained using this in situ etch back technique.

Although control of layer thickness is not easy with LPE, careful and consistent growth procedures will result in good thickness control. For example, an automated LPE method has been used to grow quantum well InGaAsP lasers with layer thicknesses of the order of 150 Å.

For the GaAlSb material, the relatively high native p-type background doping presents a special problem. In order to achieve mid-10^{15} cm^{-3} n- or p-type doped epitaxial layers, the native p-type background must be compensated with a donor atom. This problem will be covered in more detail later in the text.

2.3.2 Metalorganic Chemical Vapor Deposition

The MOCVD process that was first demonstrated by Rockwell differs from other epitaxial growth processes for III-V compounds in that the Column III metals (AlGa,In) are transported in a gaseous form to the reactor from metalorganic compounds such as trimethyl aluminum and triethylindium. These metalorganic compounds are volatile liquids which are introduced to the reactor by bubbling a carrier gas such as ultra pure hydrogen through them. In this manner, several problems associated with growth from a solution (LPE) can be avoided. In addition, problems are associated with establishing high temperature chemical equilibrium to transport the elements as gaseous hydrides such as AsH_3 and PH_3. In simplified form, the reaction may be expressed in the following way for GaAs growth.

$$(CH_3)Ga + AsH_3 \xrightarrow[700°C]{H_2} GaAs + 3CH_4 \qquad (2.3.1)$$

The vapors of the metalorganic compound are mixed with the hydride and pyrolyzed over a heated substrate. In principal, by the use of appropriate metalorganic compounds and hydrides in the right partial pressure ratio, any of the III-V compounds and alloys can be grown by this process. In fact, virtually all of the III-V compounds and most of these ternary alloys have been grown by MOCVD. The extension, for example, of the process to the quaternary $Al_{1-x}Ga_xAs_{1-y}Sb_y$ is possible and proceeds in a similar manner:

$$(1-x)\ (CH)_3\ Al + x\ (CH_3)_3\ Ga + (1-y)\ AsH_3 + y\ (CH_3)_3\ Sb \longrightarrow Al_{1-x}Ga_xAs_{1-y}Sb_y + CH_4\uparrow \qquad (2.3.2)$$

There are several distinct advantages of the general MOCVD process. Because the reactants are all gaseous, it is possible to form homogeneous gas mixtures and attain films with uniform composition. Furthermore, the composition is controlled by the partial pressures of the various constituents. These, in turn, can be precisely controlled with electronic mass flow controllers to control gas flow rates. There is no need to maintain a temperature gradient for the transport of any species and only the substrate need be heated. In addition, the kinetic properties of the reaction are not strongly dependent on temperature owing to the pyrolysis nature of the reaction.

Figure 2.3.1 shows a schematic diagram of a MOCVD growth system for the growth of GaAs and GaAlAs. The system consists of three subsystems: first, is the stainless steel gas mixing system made up of valves and tubing to control the direction and mass flow controllers to control the rate of gas flow; second is the source system consisting of stainless steel bubbler cylinders in appropriate temperature controlled baths for the introduction of the metalorganic compounds into the gas system and high pressure gas cylinders for the introduction of the hydrides and dopants. Finally, the reactor growth chamber itself consists of a quartz envelope and an inductively heated susceptor for the growth reactions which result in epitaxial crystal growth.

There are several advantages to the MOCVD process:

1. Process control is inherent with MOCVD

   Only a single hot zone, the susceptor, need be controlled. The reacting species are brought to the growth area in gaseous form. The partial pressures of these gases are controlled by electronic mass flow controllers which are part of sophisticated automated reactors designed at Rockwell that remove possible human error.

2. MOCVD provides materials and device flexibility

   A variety of III-V materials have been grown by MOCVD and utilized in sophisticated device structures. Multilayer heterojunction devices with

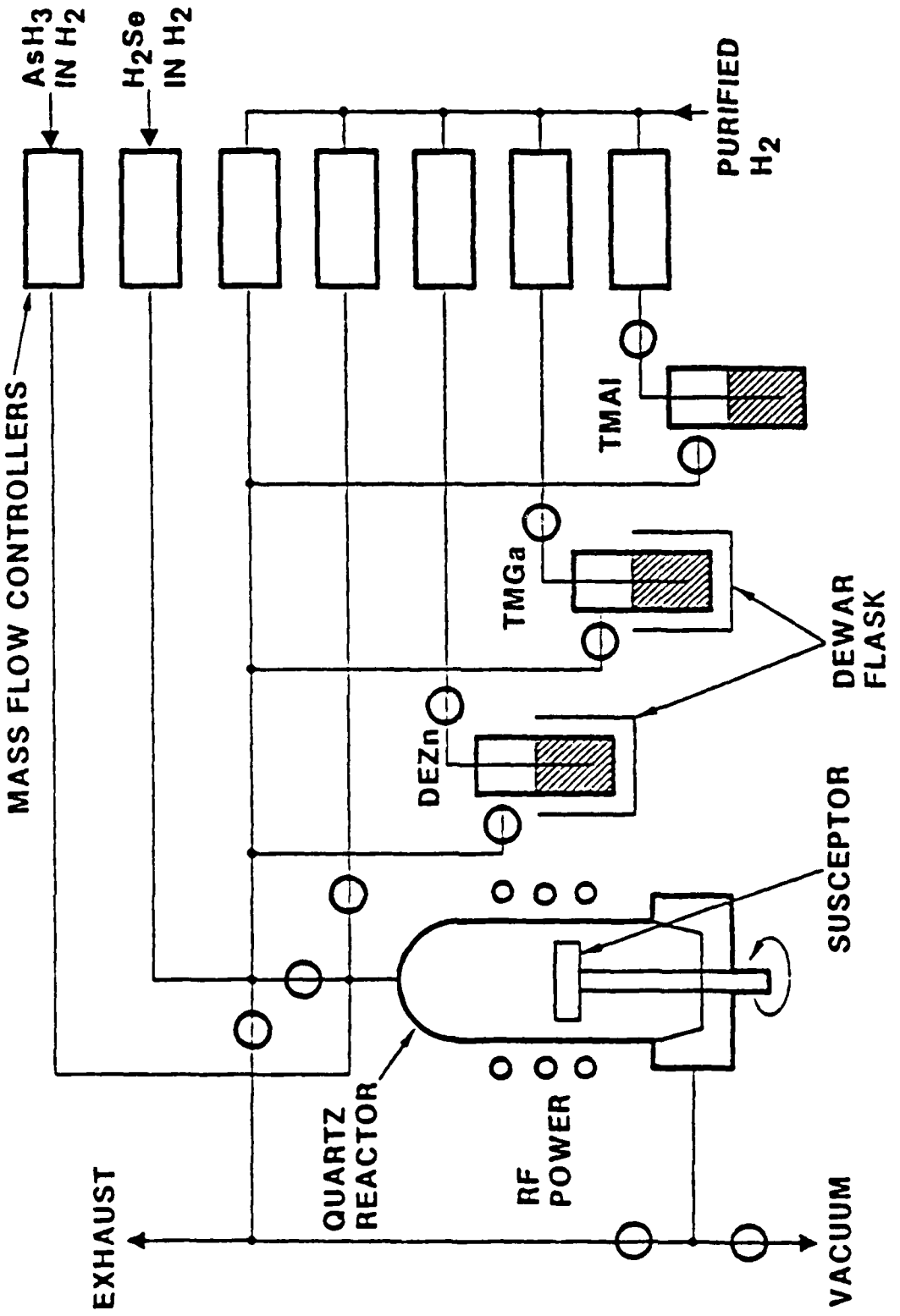

Fig. 2.3.1 Schematic diagram of a MOCVD system.

hyperabrupt interfaces have been demonstrated. In addition, the control inherent in the process has allowed the growth of uniform ultrathin epitaxial layers and structures.

3. MOCVD is scalable to large volume

   Owing to its similarity to Si epitaxial processes, it is believed that MOCVD will be scalable to comparable volumes.

4. The ability to add dilute streams of dopant gases to the main gas stream allows greater flexibility and control of the epitaxial dopant level as compared to the LPE process.

It is primarily for this final reason that GaAlSb grown by MOCVD was investigated in this study.

2.4 APD Design and Performance

2.4.1 Basic Design Consideration of an Avalanche Photodiode

An ultimate high sensitivity optical receiver consists of a low noise, high sensitivity preamplifier matched with a low capacitance, high quantum efficiency avalanche photodiode. The design of the avalanche photodiode is particularly important in obtaining the desired good matching.

The state-of-the-art preamplifier utilizing a GaAs MESFET front end and a transimpedance design has pushed the noise level to a minimum. The transimpedance design allows the optimal feedback resistance which in general for the moderate data rate (< 1 GHz) has a larger value than the standard 50 Ω input impedance. Subsequently, the Johnson noise will be reduced. The low capacitance GaAs MESFET front end will increase the sensitivity and lower the input capacitance noise of the preamplifier. The signal-to-noise ratio of an optical receiver, in general, can be written as follows:

$$\frac{S}{N} = \frac{(q\eta P_L M/h\nu)^2}{2q[(I_d + q\eta P_L/h\nu)M^2F + I_s]B + 4kT/R_F + i_c^2} \qquad (2.4\text{-}1)$$

where, q is the electronic charge, B is the bandwidth, η is the quantum efficiency of the photodiode, P_L, is the optical signal power; M, the multiplication of the diode, $h\nu$, the photon energy; I_d, the bulk dark current of the diode; F, the excess plot noise of the diode; I_s, the nonmultiplying component of the dark current; $4kT/R_F$, the Johnson noise of the preamplifier and i_c^2, the capacitance noise of the preamplifier. As we can observe from the above expression, the lowering of the Johnson noise and the input capacitance noise of the preamplifier in the denominator puts a very stringent requirement on the performance of the detector in order to have a good match between the preamplifier and the avalanche photodiode.

For the nonmultiplying surface leakage current in the photodiode, I_s should not be higher than 7×10^{-7} amp for a 150K feedback resistor ($\cong$ 30 MHz bandwidth of the amplifier). As the bandwidth requirement goes up, the feedback resistor will be reduced. Therefore, for higher data rate transmission, the surface current limitation is not as stringent, (i.e., I_s should not be higher than 1×10^{-4} amp for a 1.5K feedback design). We can conclude that the surface leakage requirement is relatively easy to satisfy.

On the other hand, the bulk leakage of the diode will be a more severe problem. As expression (2.4-1) indicates, the bulk dark current of the photodiode will directly multiply along with the optical signal increasing the noise of the system. Therefore, I_d will determine both the minimum detectable signal and the optimum operating gain of the avalanche photodiode. It is desirable to have a diode with the bulk leakage less than 1 nA to detect a nanowatt power at 100 MHz. (Of course, this depends on other factors such as excess noise factor.)

The remaining factors in designing an avalanche photodiode are the quantum efficiency, the capacitance, and the excess noise factor.

It is obvious that the higher the quantum efficiency of the diode the better is the signal-to-noise ratio, since the signal increases with η^2 while the noise increases with η. The capacitance will determine the speed and the sensitivity of the receiver. For high sensitivity at reasonable bandwidth, the capacitance should be less than 0.5 pf.

When other parameters, such as capacitance and dark current, are under control, the parameter which determines avalanche photodiode performance is the excess noise factor. The excess noise of an avalanche photodiode arises from the statistics of the avalanche process and is related to the ratio of ionization rates of the electrons and holes. The excess noise factor can be written as:

$$F = kM + 1(1 - k) - (1-k)/M \qquad (2.4\text{-}2)$$

where, k is the ratio of the ionization rate (α/β or β/α and is less than unity). The ionization rates are the material parameters. For germanium, k is approximately 1 and F is close to M which is the most undesirable case. For most of the III-V alloys, the ionization rate ratio is not as low as silicon which is approximately 0.02. In fact, the $Ga_{0.72}Al_{0.28}Sb$ alloy was found to have an ionization rate ratio of 0.5 as shown in Fig. 2.3.1. However, for this alloy system, there is a high potential to have a small k factor at lower bandgap alloy. At approximately 0.77 eV, the spin orbit splitting of the valence band is equal to the energy gap. This implies that the ionization threshold energy is at zero crystal momentum point of the energy band diagram. From experience in other resonant transitions, the probability of scattering at the resonance point is approximately two orders

of magnitude higher than the normal transitions. This will enhance the hole ionization tremendously. In fact, preliminary data show a k value of 0.05 at 1.55 microns. Due to this basic material advantage, the GaAlSb alloy is an extremely attractive candidate for APDs.

From the discussion above, the key issues for optimal device performance are:

(1) Device Capacitance

(2) Leakage Current Mechanisms

(3) Excess Noise Factor

In this program, as described in detail below, we have investigated both MOCVD and LPE growth techniques to achieve low doping densities and, therefore, low capacitance. The sources of leakage current for the composition of GaAlSb where spin orbit splitting occurs was investigated, and the influence of different device designs is discussed.

3.0 Experimental Data and Results

3.1 MOCVD GaAlSb Detector Data

As mentioned earlier and as described in the literature, for low dark current and low capacitance, net doping densities of 5×10^{15} cm^{-3} or lower must be attained. In most semiconductor material systems, this requires the use of high purity starting materials and specially developed procedures.

Owing to the native defect in the GaAlSb, the epitaxial layer doping level $N_A - N_D$ is typically in the 10^{16}-10^{17} cm^{-3} range. To convert this to the necessary $N_D - N_A$ range of $1\text{-}5 \times 10^{15}$ cm^{-3}, counter doping must be employed. Since the background native defect density is relatively high, precise amounts of the counter dopant must be added. With the native defect present, the intentionally added dopant must produce a layer which would normally be 1.1 to 1.5×10^{16} cm^{-3} n-type in any other material system. The net result will be a layer in the $1\text{-}5 \times 10^{15}$ cm^{-3} n-type range. This precise control is difficult to maintain, especially by LPE growth techniques. This factor was the prime motivation for examining GaAlSb growth by MOCVD. The experiments using this technique are now described.

Although the materials properties have been developed for the MOCVD grown AlGaAsSb material, the electronic properties are not well established. Therefore, experiments to investigate the electronic properties of AlGaAsSb as well as GaSb were performed.

For the detectors of interest in this program, it was necessary to establish whether both p- and n-type material could be grown reproducibly. When the liquid phase epitaxy process is employed, GaSb can be grown from 350 to 650°C, which is an extremely wide temperature range. In the 350 to 450°C range, unintentionally doped GaSb is n-type; in the temperature range above 450°C, the material is p-type. Whether the material is n- or p-type depends upon the number of Sb vacancies. From these data, it was thought that n-type and p-type material can be grown by MOCVD either by manipulating the growth temperature or the gas phase stoichiometry. Previously, it was shown that p-type material could be readily grown; therefore, the goal was to obtain n-type material.

A series of experiments were conducted which were designed to examine the effect of gas phase stoichiometry at different growth temperatures. The films were grown on chrome-doped GaAs or p-type GaSb. The electrical conductivity type was checked by Hall measurement (GaAs:Cr substrate) or hot-point probe. The $(CH_3)_3Ga/(CH_3)_3Sb$ flow ratio was varied from 0.198 to 0.53 which changes the stoichiometry of the crystal from antimony rich to gallium rich. The samples were checked for conductivity type by hot-point probe. The results are shown in Table I.

Table I

Sample	$(CH_3)_3Ga/(CH_3)_3Sb$*	Conductivity
GaSb- 1B19	0.53	p-type
GaSb- 2A19	0.50	p-type
GaSb- 2B19	0.46	p-type
GaSb- 3A19	0.43	p-type
GaSb- 3B19	0.40	p-type
GaSb- 4A19	0.34	p-type
GaSb-14A19	0.26	p-type
GaSb-14B19	0.198	p-type

* Reactant Molar Ratio

All the samples tested were p-type with $N_A - N_D = 5\text{-}6 \times 10^{16}$ cm^{-3}. Since no effects upon conductivity type were observed as a function of stoichiometry, the effect of growth temperature was examined. The experiments were repeated at a growth temperature of 550°C. No change in conductivity type of the grown crystal was observed as the reactant gas phase stoichiometry was varied from Ga-rich to Sb-rich. The p-type concentration was 5×10^{16} cm^{-3} as measured using Hall effect. This concentration is approximately the same as observed at $T_g = 625°C$. In addition, it was noted that the range of V/III ratio over which good surface morphology could be obtained was extremely limited. A change in the molar flow ratio of 1.38 to 1.15 changes the crystal

from gallium-rich to antimony-rich. In contrast, a similar change of ratios at 625°C resulted in little change in surface morphology. The effect that is observed here is similar to that in LPE crystal growth; as the growth temperature is decreased, the distribution coefficients increase. The net result in both systems is that composition is more difficult to control. In the gas phase system, the surface morphology degrades for small deviations in gas phase stoichiometry. The implication is that for MOCVD the growth temperature cannot be reduced further without severe alteration of gas phase stoichiometry. Since the native defect level could not be controlled using gas phase stoichiometry variation, n-type dopant in the form of H_2Se was added to the gas stream to grow n-type epitaxial GaSb. Prior to its use with GaSb, the dopant H_2Se source was calibrated by doping GaAs from 5×10^{15} to 1×10^{18} cm^{-3}.

The initial experiments demonstrated that n-type GaSb could be successfully grown by MOCVD. From Hall measurements performed by an n-type GaSb epilayer grown upon semi-insulating GaAs, a carrier concentration of $N_D - N_A \sim 1 \times 10^{17}$ cm^{-3} was obtained. The measured 300K Hall mobility was only 357 $cm^2/V\text{-sec}$. Due to the low mobility value obtained, a decision was made to characterize n-type GaSb grown upon undoped (p-type) GaSb substrates. In this way, interfacial phenomena due to the lattice mismatch are eliminated. The data obtained from Hall measurements on these samples were inconclusive due, most likely, to the fact that the p-substrate could not be grounded during this measurement.

An alternate method of epilayer-substrate isolation was devised which consisted of growing an undoped AlSb buffer layer 1 micron thick prior to deposition of the n-type GaSb. The GaSb/AlSb/GaSb (substrate) sample was grown under slightly different conditions from the GaSb/GaAs:Cr sample. Characterization by Hall measurement indicated a carrier concentration, $N_D - N_A$, of 2×10^{17} cm^{-3} with a mobility of 1200 to 1250 cm^2/V-sec at 300K. For a sample of GaSb/AlSb/GaSb (substrate) grown with the same conditions as the above described GaSb/GaAs:Cr sample, a p-type carrier concentration of 1×10^{18} cm^{-3} was obtained. Due to the large dispersion in the data, no conclusion could be drawn about the influence of growth conditions on the quality of the epilayer.

Schottky barriers were also deposited upon n-type MOCVD grown GaSb. The breakdown voltages of these devices indicated n-type doping densities of mid 10^{17} cm^{-3}. Photoresponse was observed on these devices.

These results indicated that substantial further work was required to produce material by MOCVD suitable for the fabrication of avalanche photodiode detectors. Therefore, it was decided to pursue a course of development with primary emphasis upon material grown by LPE techniques.

The standard LPE growth technique, as described earlier, was employed in this program. The gallium and GaSb were baked in a prepurified hydrogen ambient at 600°C for 18 hours prior to loading of the substrate, dopant, and aluminum wire. After all constituents had been loaded, the furnace was heated to

560°C, and the aluminum wire was allowed to mix with the gallium. After approximately one hour, the furnace temperature was cooled to 550°C, and the crystal growth was initiated. The majority of the substrates used in these experiments were n-type tellurium doped GaSb.

3.2 Tunneling Data

As pointed out earlier, leakage current can be detrimental to photodiode performance. The seriousness of the problem depends on the detector application and the type of leakage source and its relative contribution to the total dark current. In this section, we examine the sources of dark current and their impact upon device performance. This will be done for 1.3 micron and 1.55 micron GaAlSb avalanche photodetectors.

The effect of leakage upon the signal-to-noise ratio depends critically upon the nature of the leakage mechanisms. This is clearly seen in the expression given by McIntyre:

$$\frac{S}{N} = \frac{(q\eta PM/h\nu)^2}{2qB[(I_D + q\eta P/h\nu)M^2 f(M) + I_s] + 4K_B T/R_L + (\text{Amplifier noise})} \quad (3.2\text{-}1)$$

where the I_D consists primarily of three components

$$I_D = I_{GR} + I_{db} + I_{TUN}$$

I_{GR}: Leakage due to generation recombination

I_{db}: Leakage due to diffusion

I_{TUN}: Leakage due to tunneling which occurs at high electric fields

and I_s: Dark current due to surface leakage.

As is evident, the surface leakage does multiply with the gain (M). Although surface leakage does not effect avalanche gain, it does effect photodetector sensitivity.

The primary leakage mechanism ascribed to GaSb devices prior to the work performed here was surface current. If surface leakage is the dominant dark current mechanism, its further reduction through design or otherwise should yield excellent photodetectors. This raised a fundamental question: "Is there another leakage mechanism in operation that would still limit the avalanche gain even after the surface leakage had been eliminated?" This question is answered here.

In this section, we describe measurements of the dark current of GaAlAsSb ($E_g \sim 0.9$ eV) APDs as a function of temperature which indicated that the reverse current for these devices can be dominated by trap assisted tunneling.

The GaAlAsSb/GaSb structures of interest were grown by the LPE process. The doping densities of the grown n-type layers were in the range from 3×10^{15} cm^{-3} to 4×10^{16} cm^{-3}. The p-n junction was formed using Be-implantation. For the devices used for the tunneling measurements, isolation between the devices was provided by mesa etching.

For the measurement of the I-V characteristics as a function of temperature, a closed cycle cryogenic refrigerator (Lake Shore Model 21SC) was used to cool the diodes. Once at the desired temperature, the I-V characteristics were measured by applying a staircase voltage with 0.2 volt steps and measuring the resulting reverse current at each voltage using an HP 4041A pA meter/voltage source. An HP 9845A desktop computer was used both for automatic control of the experiment and for data analysis. The I-V measurements were made at 20°K intervals over the temperature range from 80 to 320°K. Several representative I-V plots are shown in Fig. 3.2.1.

The reverse current at low bias voltages is attributed to generation and recombination of carriers in the exposed depletion region at the surface of the device. It can be described by

$$I_{g-r} = I_0 \cdot V^m \qquad (3.2\text{-}2)$$

with $m \cong 3/4$ and for V greater than several kT/q. As will be shown below, at higher voltages, a tunneling component dominates until avalanche breakdown occurs. The avalanche breakdown voltage decreases with decreasing temperature, indicating a stronger dependence of this parameter on hot carrier scattering than on bandgap variation as is commonly observed for III-V semiconductor alloys.

The exact expression for the tunneling current depends on the barrier model chosen. The functional dependence of the tunneling current on reverse bias

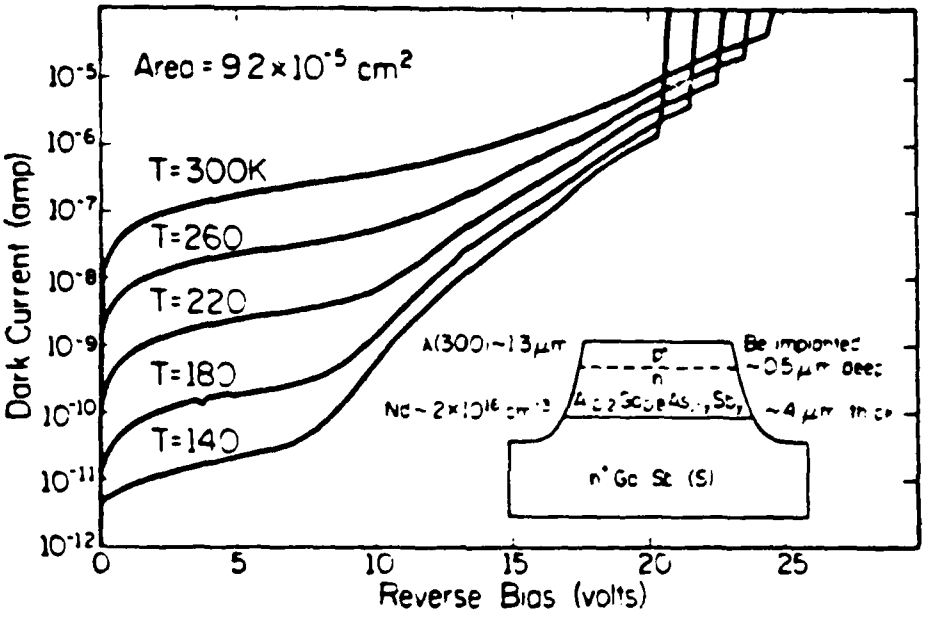

Fig. 3.2.1 Temperature dependent I-V characteristic of Be-implanted GaAlSb photodiode

voltage and electric field, however, remains the same for different models. Moll gives the reverse tunneling current for band-to-band tunneling in direct bandgap semiconductors as

$$I_{tun} = \frac{\sqrt{2}\, Aq^3 m^{*1/2} F_{max} F}{4\pi^3 h^2 E_g^{1/2}} \exp\left(-\frac{\pi m^{*1/2} E_g^{3/2}}{2\sqrt{2}\, qhF_{max}}\right) , \qquad (3.2\text{-}3)$$

where A is the device area and F_{max}, the maximum electric field, is given by

$$F_{max} = \left(\frac{2qN_d V}{\varepsilon}\right)^{1/2} \qquad (3.2\text{-}4)$$

Tunneling is also possible via energy states (traps or defects) within the forbidden energy gap. Defect assisted tunneling is expected to retain the same functional form as band-to-band tunneling, but the tunneling probability in this case depends on the density of the defects. The tunneling energy or barrier height will also be reduced from E_g. Therefore, we may define an effective tunneling energy, T_{tun}, which is equal to E_g for band-to-band tunneling and smaller than E_g for defect assisted tunneling.

The substitution of Eq. (3.2-4) in Eq. (3.2-3) gives the voltage dependence of the tunneling current as

$$I_{tun} = C_1 \cdot V^{3/2} \cdot \exp(-C_2/V^{1/2}) , \qquad (3.2\text{-}5)$$

where all of the factors not involving the bias voltage have been aggregated into two, namely C_1 and C_2. The result is a general expression for all

the barrier models which includes defect assisted tunneling. The constant C_2 is proportional to $(E_{tun})^{3/2}$, and this dependence is utilized below to estimate E_{tun}.

The tunneling current component was determined by subtracting I_{g-r} from the total dark current, I_D. A plot of log $[(I_D - I_{g-r})/V^{3/2}]$ vs $V^{-1/2}$ should yield a straight line with a slope of C_2 and y-intercept of log C_1. In fact, excellent fits were obtained up to about five to six volts below the avalanche breakdown voltage V_B. For voltages greater than V_B-5 volts but less than V_B, the current is larger than predicted. The source of this excess current will be discussed below. From the fits to these data, it is possible to estimate the tunneling energy, E_{tun}. The equation for C_2 is

$$C_2 = K\, m^{*1/2}\, E_{tun}^{3/2}\,, \qquad (3.2\text{-}6)$$

where K is constant with T, and

$$(C_2)^{2/3} = K^{2/3}\, m^{*1/3}\, E_{tun}\,. \qquad (3.2\text{-}7)$$

Taking the derivative with respect to temperature gives

$$\left[\frac{d}{dT}\,(C_2)^{2/3} = K^{2/3}\,\left(E_{tun}\,\frac{d}{dT}\,m^*\right)^{1/3} + m^{*1/3}\,\frac{d}{dT}\,E_{tun}\right]\,. \qquad (3.2\text{-}8)$$

If we ignore the small temperature variation of $(m^*)^{1/3}$, equations (3.2-7) and (3.2-8) give

$$E_{tun} \cong \frac{(dE_{tun}/dT)}{[d(C_2)^{2/3}/dT]} \times (C_2)^{2/3} \quad . \qquad (3.2\text{-}9)$$

The variation of $(C_2)^{2/3}$ with T as determined from the fits to Eq. (3.2-5) as described above is shown in Fig. 3.2.2. At 300°K,

$$(C_2)^{2/3} \cong 13.4 \text{ volts}^{1/3} \qquad (3.2\text{-}10)$$

and

$$\frac{d}{dT} (C_2)^{2/3} = 2 \times 10^{-2} \text{ volts}^{1/3} \text{ K}^{-1} \quad . \qquad (3.2\text{-}11)$$

If we approximate dE_{tun}/dT by the band-to-band value using the energy gap variation with temperature given by Pankove,

$$\frac{d}{dT} E_g(\text{GaAlAsSb}) \cong \frac{d}{dT} E_g(\text{GaSb}) \cong \frac{d}{dT} (\text{AlSb}) \cong 4 \times 10^{-4} \text{ eV K}^{-1} \qquad (3.2\text{-}12)$$

we can estimate E_{tun} using Eq. (3.2-9) as

$$E_{tun} \cong 0.27 \text{ eV} \qquad (3.2\text{-}13)$$

This value is much less than the energy gap for this material, $E_g = 0.95$ eV, and suggests that the tunneling current results from defect assisted tunneling. It should be noted that the tunneling barrier for electrons trapped at a defect can be reduced from the defect energy level because of the

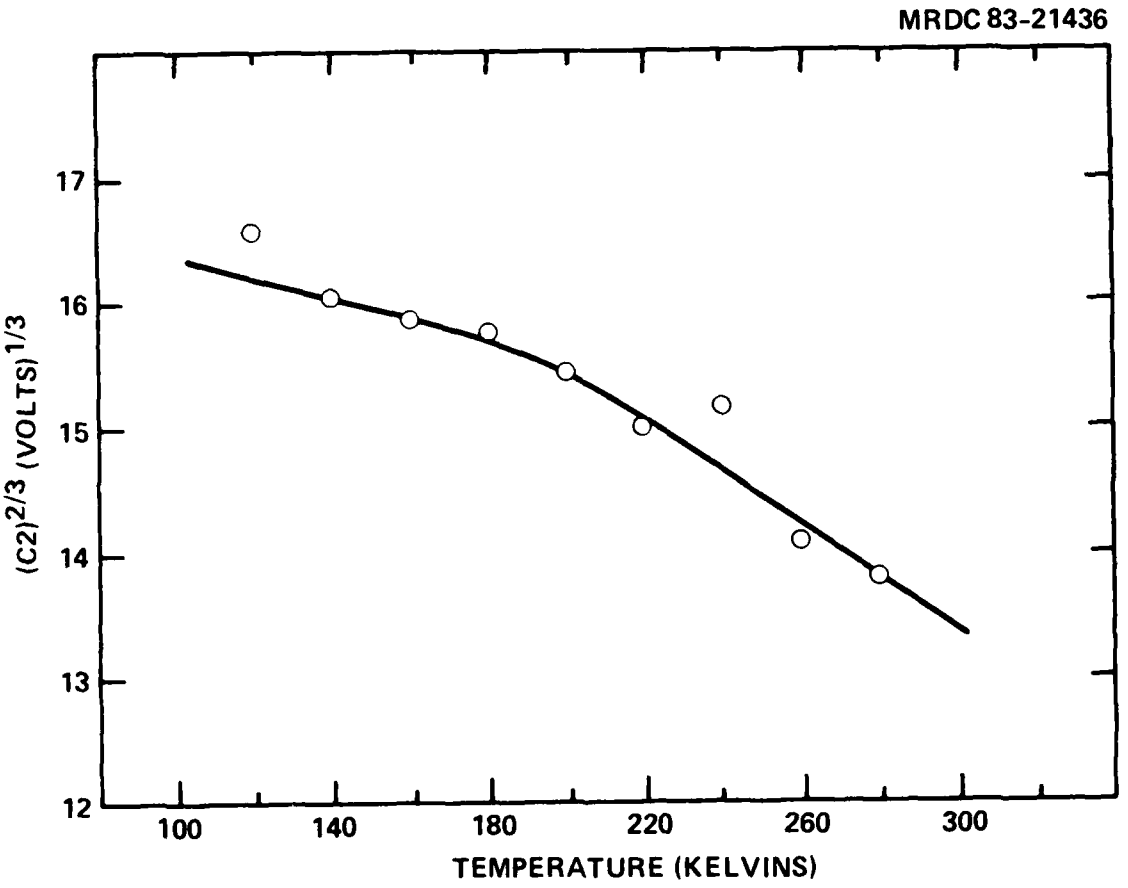

Fig. 3.2.2 The variation of $(C_2)^{2/3}$ with temperature.

influence of both the electric field and phonon assisted processes, even for traps with non-coulombic potentials.

Figure 3.2.3 shows that, when I_{g-r} and I_{tun} are subtracted from the total dark current, a third component appears. The bias and temperature dependence of this component is very similar to the dominant tunneling component. However, this component has a much larger E_{tun} value when compared to that of the dominant tunneling component. The appearance of the third component of the leakage current at very high electric fields strongly suggests the onset of band-to-band tunneling. Calculations by Takanashi and Horikoshi show that, for GaAlSb of doping $N_D \sim 2 \times 10^{16}$ cm^{-3} and bandgap $E_g \sim 0.97$ eV, the material lies in the region of Zener breakdown, yet is extremely close to the transition between Zener dominated breakdown and avalanche breakdown. The temperature dependence of the breakdown, as shown in Fig. 3.2.1, however, clearly demonstrates that avalanche multiplication is definitely the dominant breakdown mechanism. Comparing InGaAsP to GaAlSb, the transition from avalanche dominated breakdown to tunneling dominated breakdown (Zener) occurs at a higher doping density for GaAlSb owing to its higher effective electron mass.

Although the defect assisted tunneling allows avalanche action to occur, it does seriously degrade the sensitivity of the detector. There is also the possibility that implantation residual damage still remains in the crystal and is the source of defect assisted tunneling current.

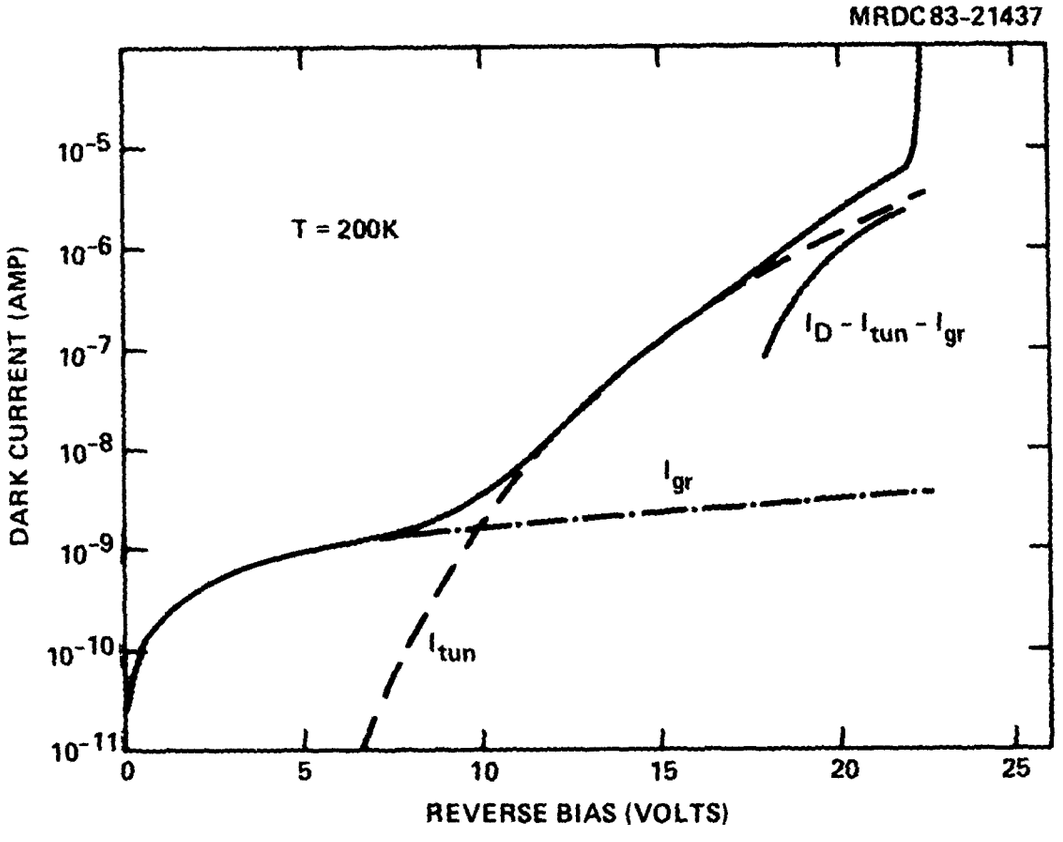

Fig. 3.2.3 Dark I-V showing I_{g-r} and I_{tun}.

In the next section, 1.55 micron GaAlSb Schottky barrier photodiodes are examined. No implantation process was employed in the fabrication of these devices. The sources of dark current and the gain characteristics are studied.

3.3 1.55 Micron GaAlSb Avalanche Photodetectors

As pointed out previously, the GaAlSb materials system offers the possibility for avalanche photodetectors having low noise avalanche gain at a composition of $Ga_{0.94}Al_{0.06}Sb$. In Figure 3.3.1, we show in an X-ray rocking curve that the GaAlSb grown at Rockwell has a composition of $Ga_{0.94}Al_{0.06}Sb$. Note that the line width of both curves are approximately equal. This indicates the crystalline quality of the epitaxial layer is comparable to that of the substrate. A confirmation of composition is shown by the photoresponse measurement of Fig. 3.3.2. The exponential drop in photocurrent at the wavelength of 1.55 micron indicates the GaAlSb epitaxial layer has a AlSb mole fraction of 0.6. This corresponds to a bandgap of $E_g \sim 0.8$ eV.

In addition to the lattice calibration, doping levels must be accurately calibrated to obtain the necessary breakdown voltage and electric field strength to have avalanche gain. In our work, this step has proven to be difficult and subject to variations on a run-to-run basis. The primary cause of this, as indicated earlier, is the p-type native defect has a carrier concentration of 1-5 x 10^{16} cm^{-3} typically. This must be compensated by an intentionally added n-type donor. By controlling accurately the n-type

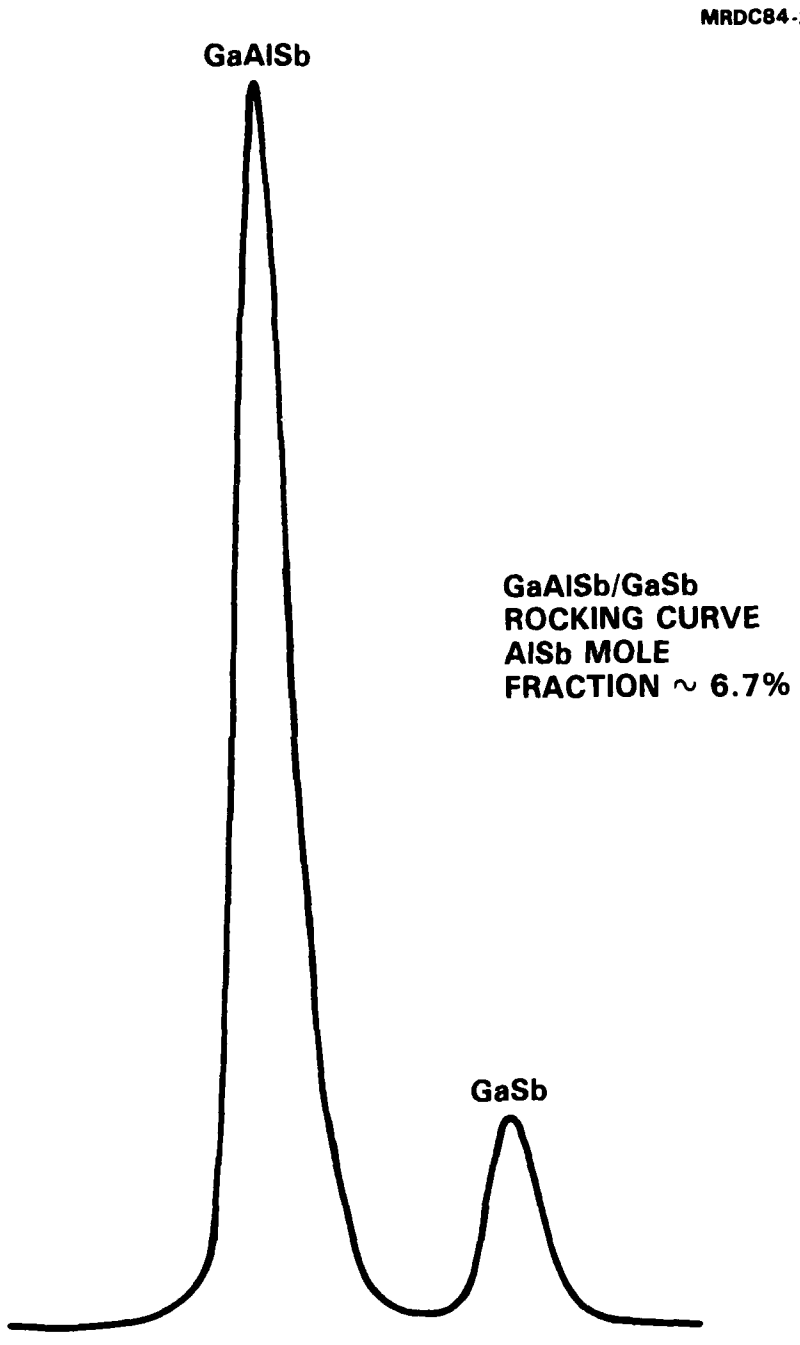

Fig. 3.3.1 Rocking curve of a GaAlSb epilayer grown upon GaSb.

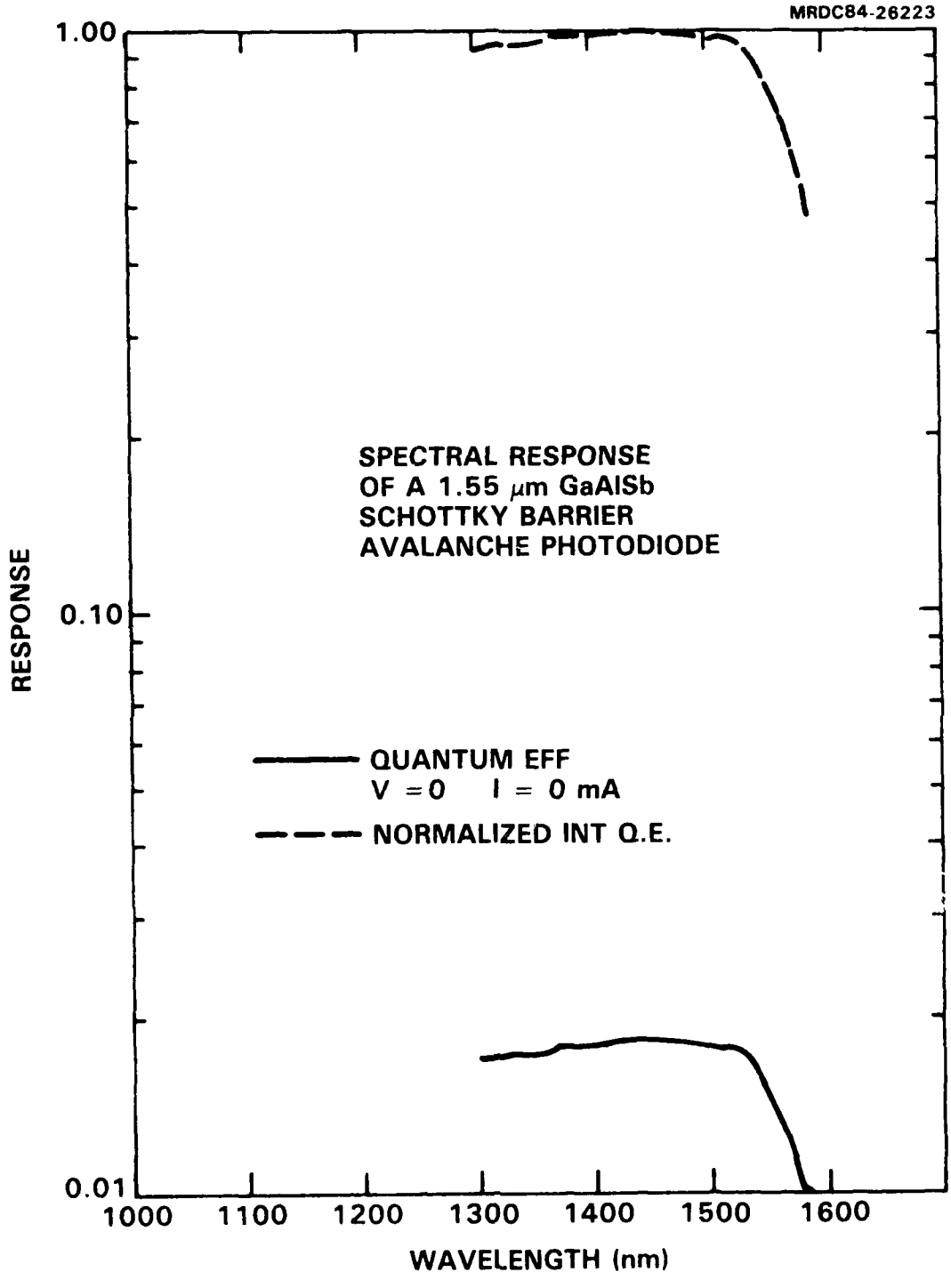

Fig. 3.3.2 Photoresponse vs. wavelength of a Schottky barrier GaAlSb avalanche photodetector.

impurity level, $N_D - N_A$ levels of mid to high-10^{15} cm^{-3} can be obtained leading to high electric fields and breakdown voltages. Using this procedure, breakdown voltages of Schottky barrier devices, in excess of 40 volts, have been fabricated. The doping is estimated using the following equation,

$$V_B \cong 60(E_g/1.1)^{3/2} (N_B/10^{16})^{-3/4} \text{ V} \qquad (3.3.1)$$

Solving for N_B, we obtain $N_B \sim 8\text{-}9 \times 10^{15}$ cm^{-3} for $V_B \cong 40\text{-}45$ volts. With the doping and composition calibrated, Schottky barrier detectors were fabricated.

Shown in Fig. 3.3.3 is the dark and illuminated I-V characteristic of a Schottky barrier avalanche photodiode using two different scales (i.e., 10^{-5} and 10^{-4} amps). It is evident from these curves that optical gain is observed. This fact is of major importance, since avalanche operation occurs at a doping level which far exceeds that necessary to have avalanche gain in InGaAsP of comparable bandgap. In other words, the calculated maximum level of doping to obtain avalanche gain is approximately $N_D - N_A \sim 8 \times 10^{15}$ cm^{-3}. The calculated donor density required for avalanche gain in comparable bandgap InGaAsP is $N_D - N_A \sim 9 \times 10^{14}$ cm^{-3}. Optical gains as high as 30 have been observed before the onset of substantial dark current above that obtained at low voltages.

Figure 3.3.4 shows the photoresponse of the detector to a linear light scan. The traces correspond to different operating voltages. The spacial response is broken into three regions, I, II, and III. In region I, we have

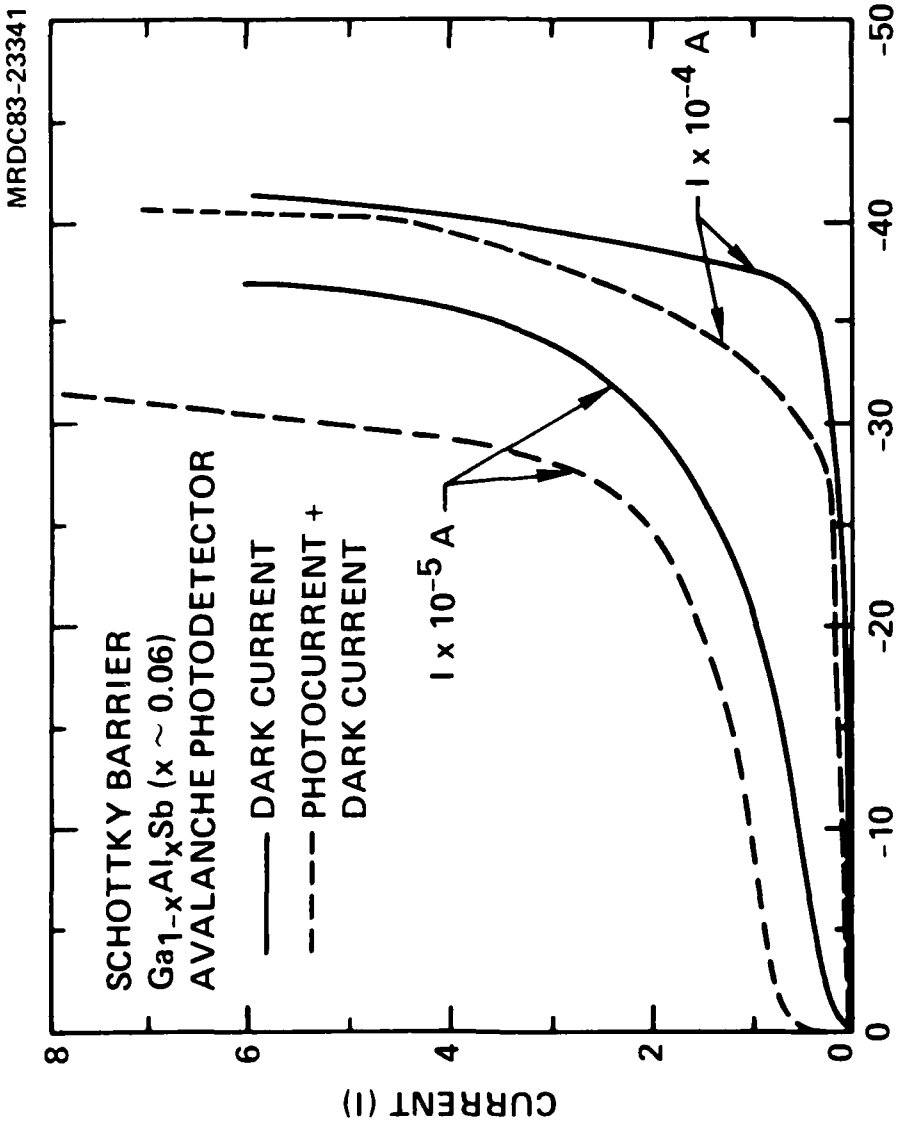

Fig. 3.3.3 Dark and illuminated I-V characteristic of a Schottky barrier avalanche photodiode showing gains in excess of thirty.

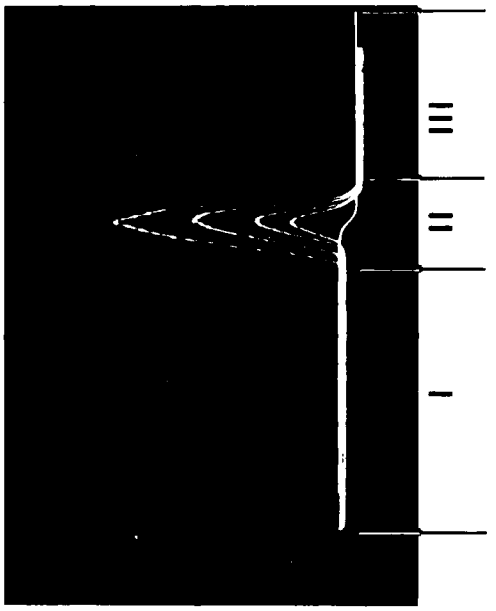

Fig. 3.3.4 Photoresponse of the device of Fig. 3.3.3 to a linear light scan

photoresponse at unity gain. Region II shows the effect of the operating voltage upon the gain characteristics. Finally, region III is the area beneath the Au Schottky barrier and shows no response to the illumination beam. As expected, gain is obtained in region II where the electric field is extremely high.

An interesting point in this photograph is the photoresponse observed many mils beyond the perimeter of Schottky barrier. Carriers generated by the optical excitation are being collected probably in a surface depleted channel and are subsequently collected at the Schottky contact. This observation has a tremendous implication for detectors designed from this material. If a structure has n-type GaSb or GaAlSb as a surface, the inversion at the surface must be eliminated. In a p-n junction detector structure, this can be accomplished by using a p-type substrate and depositing an n-type epitaxial layer. Defining mesas that are etched to the substrate will result in the elimination of large n-type surface inversion layers.

The prominent feature of this device is that avalanche gain is observed. At this bandgap ($E_g \cong 0.8$ eV) and impurity level ($N_D - N_A \cong 8\text{-}9 \times 10^{15}$ cm^{-3}), calculations by Takanashi and Horikoshi show that this material should be in the Zener dominated breakdown region. To further ensure that the breakdown process is due to avalanche ionization, the temperature dependent I-V characteristics were examined. Figures 3.3.5, 3.3.6, and 3.3.7 show the results from two different GaAlSb Schottky barrier avalanche photodiodes. For an avalanche dominated breakdown, the breakdown decreases with decreasing

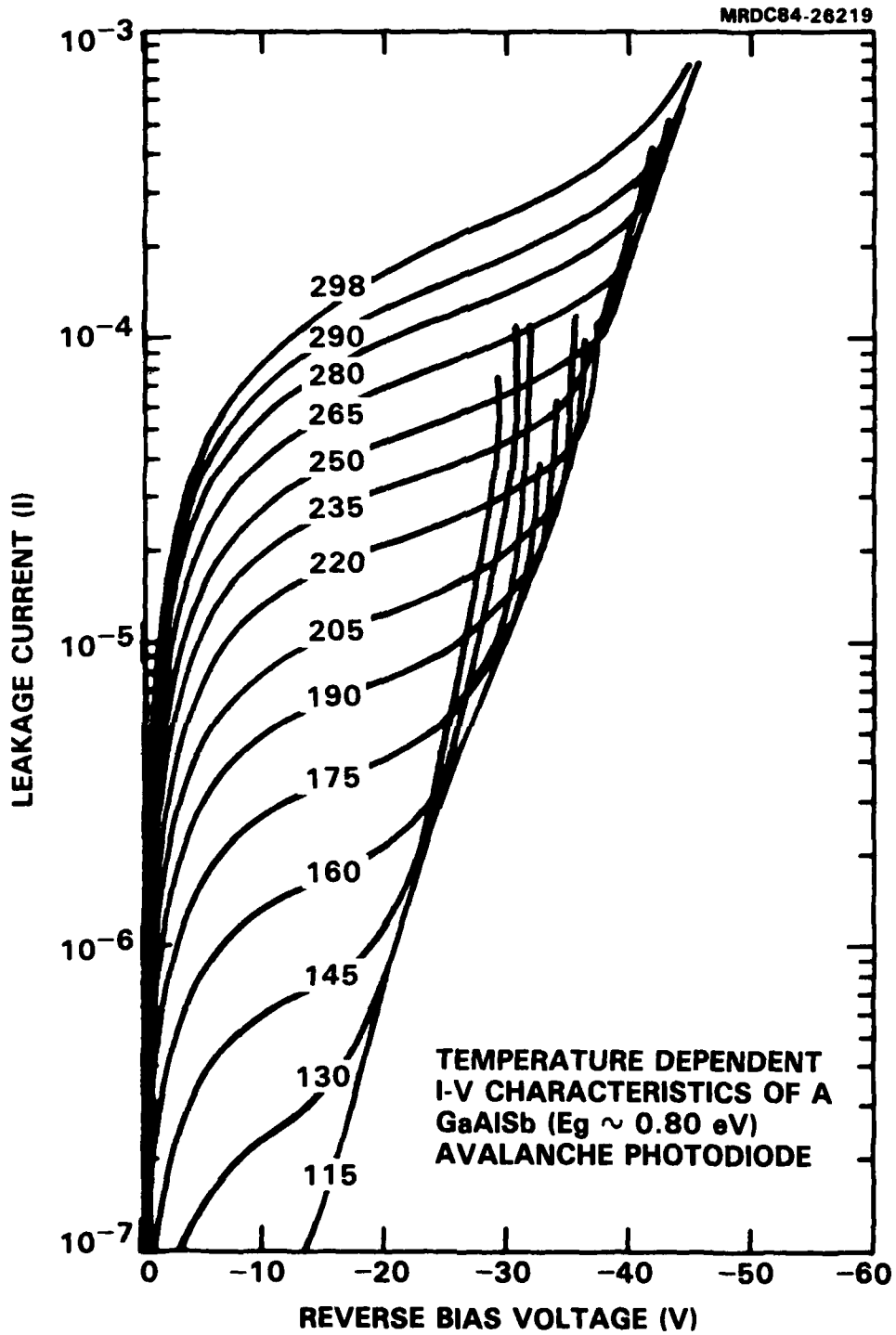

Fig. 3.3.5 Temperature dependent I-V characteristics of a GaAlSb ($E_g \cong 0.80$ eV) avalanche photodiode.

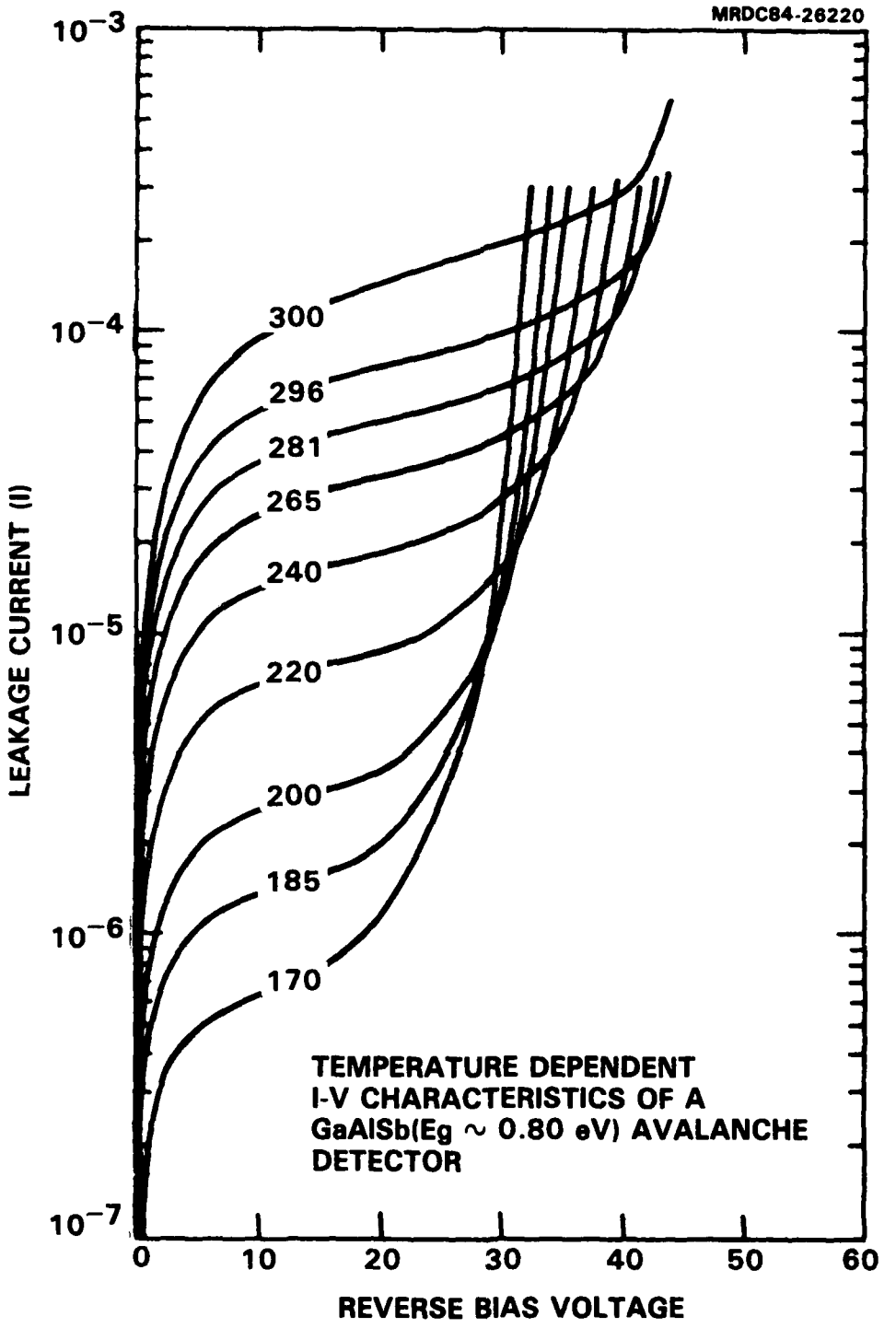

Fig. 3.3.6 Temperature dependent I-V characteristic of a second GaAlSb ($E_g \cong 0.80$ eV) avalanche photodiode.

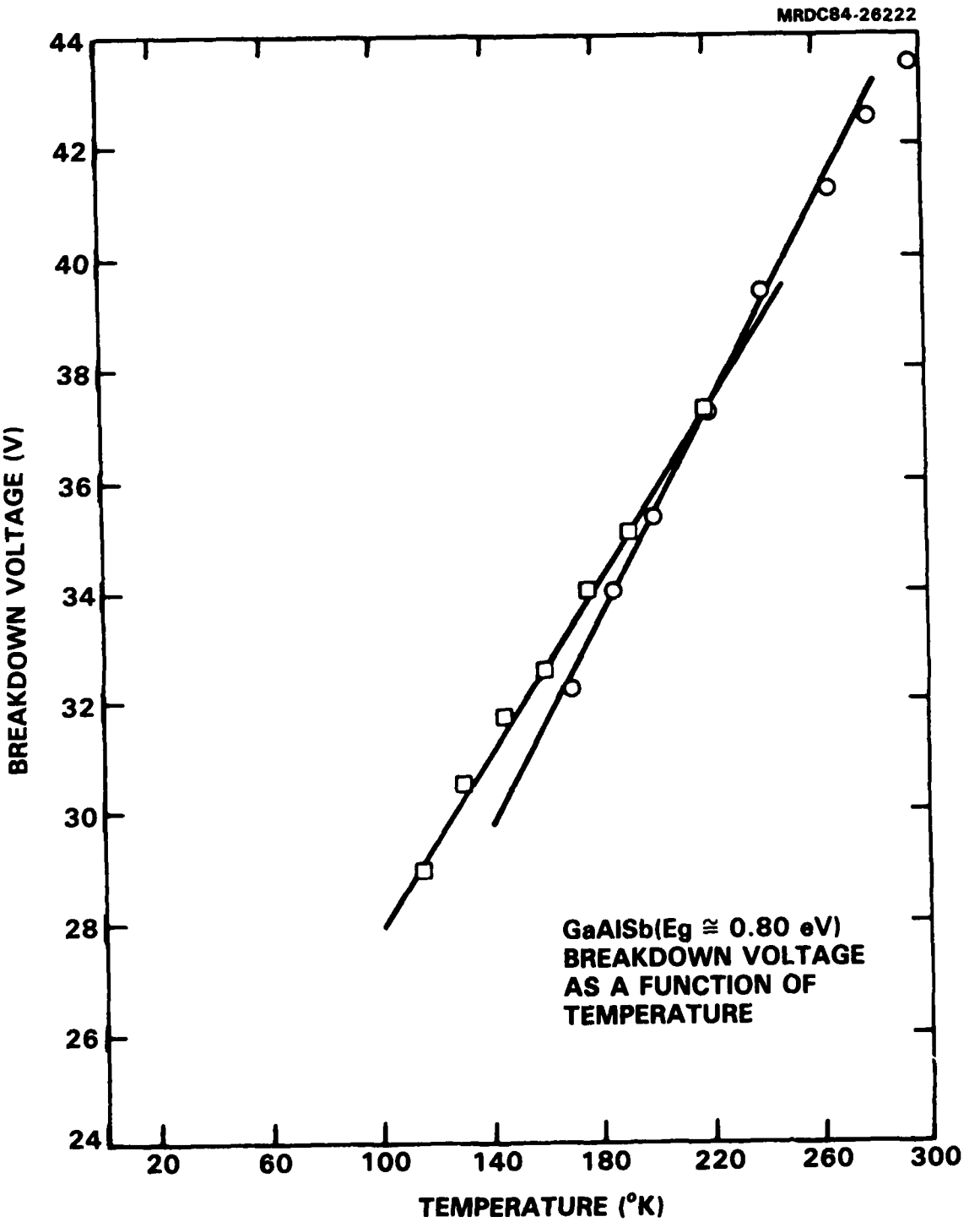

Fig. 3.3.7 GaAlSb Schottky avalanche breakdown voltage as a function of temperature

temperature. Figures 3.3.5-3.3.7 show clearly this is the case. Obviously, much higher impurity level GaAlSb avalanche photodetectors can be fabricated compared to InGaAsP avalanche photodiodes of comparable bandgap. This also indicates that the tunneling observed in InGaAsP under moderate to high field conditions may not be direct band-to-band tunneling.

The temperature dependent I-V characteristics of these GaAlSb ($E_g \sim 0.80$ eV) Schottky barrier avalanche photodiodes can be compared to the previous Be-implanted devices for tunneling characteristics. Since the surface leakage can be reduced with temperature, the bulk leakage may be studied directly. This is complicated by the fact that a surface inversion exists in this material. By assuming that the total surface area of leakage contribution is constant, we can draw some useful conclusions about the bulk leakage phenomenon. From the I-V characteristics of Fig. 3.3.5 and 3.3.6, it is evident that such an assumption is not unreasonable. Surface leakage which is a generation-recombination process should follow a similar curve as in Fig. 3.2.3. In this case, the fact that another component completely dominates the characteristic at higher electric field justifies our assumption.

The domination of the reverse current characteristic by an unknown component prior to avalanche breakdown is the area we will now discuss.

As is evident from the family of curves of Figures 3.3.5 and 3.3.6, the surface leakage and bulk generation-recombination decreases rapidly with temperature. Normally, the reverse current characteristic would follow the

generation-recombination curve until avalanche breakdown occurs. For these devices, however, another leakage mechanism appears at medium to high electric fields. This is clearly seen in Figure 3.3.8. This is the same device of Figure 3.3.5. The leakage increases exponentially between the reverse bias voltages of 14 and 23 volts. This dark current source increases the total leakage by two orders of magnitude, near breakdown, beyond what would be obtained from pure generation-recombination dark current. Although they are not as pronounced, the curves of Figures 3.3.5 and 3.3.8 have the same general form as the curves of Figure 3.2.3. Both the defect tunneling characteristics and the additional dark current prior to the onset of avalanche multiplication occur. These are more readily apparent on the low temperature curves of Figure 3.3.5 and Figure 3.3.8 than on Figure 3.3.6.

The contribution to dark current by the defect assisted tunneling source is much greater than that observed on the GaAlSb Be-implanted device. This may be caused by a higher density of defect states. It is known for the GaAlSb material that the p-type native defect level decreases with increasing bandgap. The other possibility may be that the Schottky barrier device has a greater density of states in the bandgap at the surface, thereby increasing the total tunneling current. Regardless of the mechanism, the fact remains that tunneling has been observed in two major types of GaAlSb avalanche photodiodes. In addition, the tunneling currents seriously degrade the sensitivity performance of these devices.

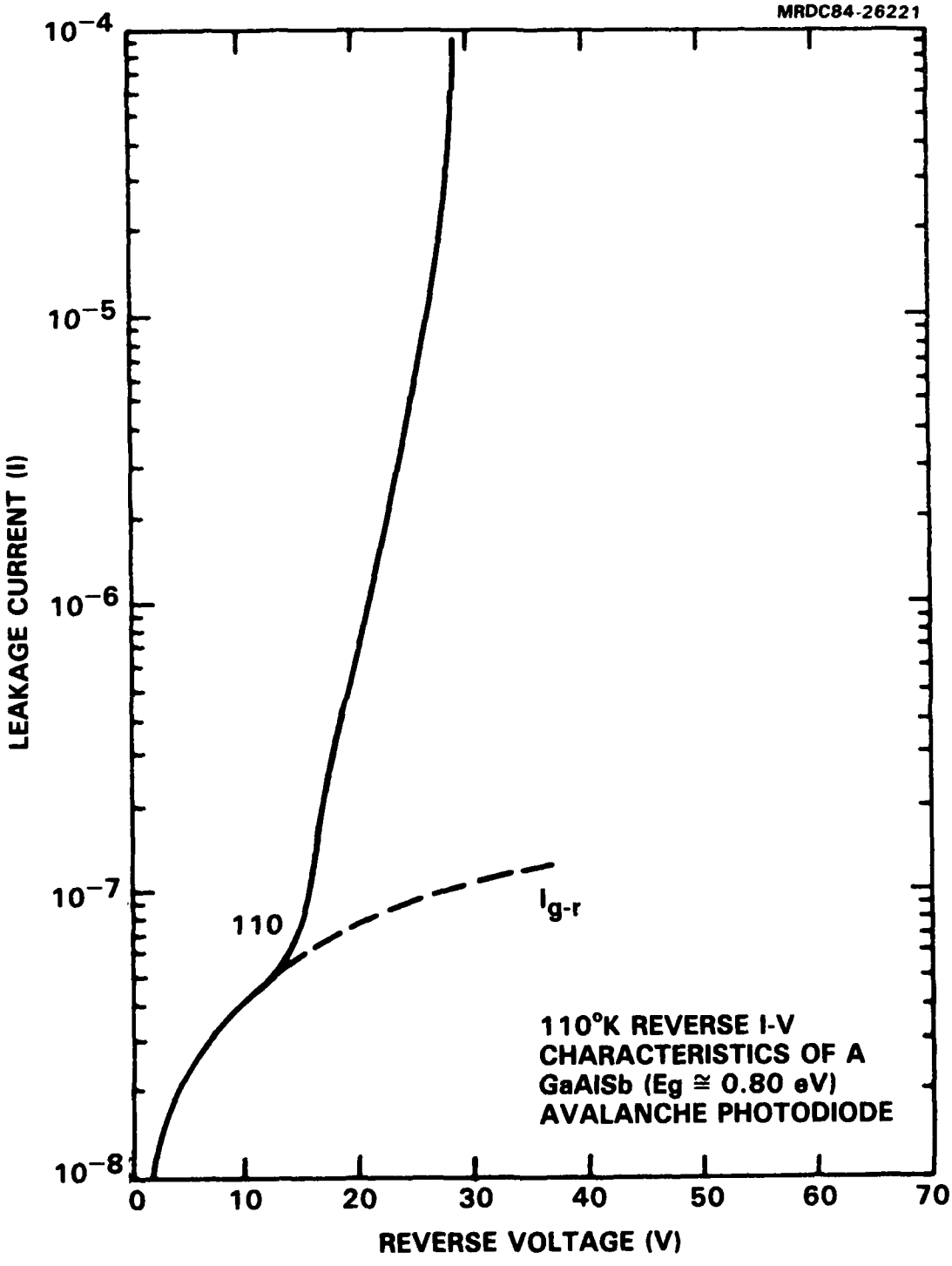

Fig. 3.3.8 110°K reverse I-V characteristic of a GaAlSb ($E_g \cong 0.80$ eV) avalanche photodiode.

Although avalanche photodiode configurations have been devised which will reduce the surface leakage contributions, the bulk tunneling current will remain a severe problem.

4.0 Summary

It has been demonstrated that avalanche gain can be obtained in 1.55 μm GaAlSb avalanche photodiodes which have the ionization coefficient enhancement. These devices exhibit gain at a relatively high impurity background density of 8-9 x 10^{15} cm^{-3}. This indicates tunneling which occurs in these GaAlSb photodiodes occurs through a deep level rather than through a band-to-band process. Surface leakage current which dominates the total dark current at room temperature can be reduced with the use of special structures; however, as shown in this work, defect assisted tunneling may be a fundamental limitation to obtaining high sensitivity devices. One other serious problem from the manufacturing standpoint is the necessity to compensate the native defect which results in high intrinsic p-type acceptor levels. Precise dopant control is required to obtain reproducible impurity levels.

MISSION
of
Rome Air Development Center

RADC plans and executes research, development, test and selected acquisition programs in support of Command, Control Communications and Intelligence (C^3I) activities. Technical and engineering support within areas of technical competence is provided to ESD Program Offices (POs) and other ESD elements. The principal technical mission areas are communications, electromagnetic guidance and control, surveillance of ground and aerospace objects, intelligence data collection and handling, information system technology, ionospheric propagation, solid state sciences, microwave physics and electronic reliability, maintainability and compatibility.

Printed by
United States Air Force
Hanscom AFB, Mass. 01731

END

FILMED

2-85

DTIC